steel research international
www.steel-research.d

Steel Alloy Homogenization During Rheinsahl–Heraeus Vacuum Treatment: Conventional Computational Fluid Dynamics, Recurrence Computational Fluid Dynamics, and Plant Observations

Stefan Pirker, Stefan Puttinger, Roman Rössler, and Thomas Lichtenegger*

Computational fluid dynamics (CFD) simulations of steel flow in an Rheinsahl–Heraeus (RH) process are realized by a discrete phase model (DPM) for the driving bubble plumes, a volume of fluid (VoF) method for the free surface in the vacuum chamber (VC), and a large eddy simulations (LES) model for the transport and mixing of steel alloys. CFD simulations are opposed to particle image velocimetry (PIV) analyses of flow pattern at the bath surface in the VC. While simple Reynolds averaged turbulence models fail to reproduce these plant observations, LES agrees fairly well. Furthermore, the steel recirculation rate is compared with empirical correlations from the literature, yielding good agreement with respect to the dependency of the recirculation rate on the gas injection rate. The absolute value of the recirculation rate increases by 15%, in case (realistic) eroded edges are considered instead of a (unrealistic) sharp-edged geometry. Data-assisted recurrence CFD (rCFD) is applied to accelerate conventional CFD. The rCFD simulations yield a computational speed-up of four orders of magnitude, enabling real-time LES at full grid resolution of three million cells. Titanium homogenization in the steel ladle is addressed by means of rCFD and compared with corresponding plant trials yielding good agreement.

1. Introduction

Vacuum processes (e.g., Rheinsahl–Heraeus (RH) process) enhance metallurgical reactions that comprise a gaseous reaction product (e.g., decarburization, removal of nitrogen or hydrogen). In an RH plant, liquid steel is lifted up into the vacuum chamber (VC) by two snorkels. In the up-leg snorkel, argon is additionally introduced by a set of nozzles to drive a global recirculating flow pattern (**Figure 1**). During operation, steel with high concentration of dissolved gases is guided through the up-leg into the VC. After passing the VC, refined steel flows back to the ladle through the down-leg. In addition, steel alloys can be introduced into the VC, which subsequently homogenize in the steel ladle by the global steel recirculation flow.

With many metallurgical processes, the RH process is hardly accessible to detailed measurements (due to the hot environment, opaque liquids, and thick walls). In estimating the recirculation rate, researchers commonly rely on experiments of global alloy dissolution or semianalytical considerations. As a result, several empirical correlations for the recirculation rate have been proposed.[1–4] Most of them include the influence of the main geometrical features of the plant as well as the gas flow rate and in some cases the pressure inside the VC. Recirculation models have also been combined with compartment models, which differentiate between kinetic reaction mechanism in the VC and species mixing in the ladle.[5]

Other researchers pictured the RH process by cold water models, studying main flow features, recirculation rate, and species mixing.[6,7] They concluded that a dominant immerged jet is formed in the ladle, just below the down-leg of the VC. Such water models also serve as validation basis for numerical simulations of different level of complexity. Geng et al.,[8] for instance, considered 3D recirculation flow, neglecting surface deformations in the VC. More recently, Ling et al.[9] applied a free-surface volume of fluid (VoF) model in combination with a discrete phase model (DPM) for the rising bubble plumes, thus considering the most dominant multiphase flow features. For modeling species mixing in the ladle, commonly unsteady Reynolds-averaged Navier–Stokes (URANS) models have been used.[10] From a fluid dynamical perspective, this raises concerns because it is accepted in the literature that simple URANS turbulence models such as the standard $k-\varepsilon$ model are not able to predict the flow of a submerged round jet, which obviously represents a key feature of ladle flow.[11] Furthermore, visual

Prof. S. Pirker, Dr. S. Puttinger, Dr. T. Lichtenegger
Department of Particulate Flow Modelling
Johannes Kepler University
Altenbergerstraße 69, 4040 Linz, Austria
E-mail: Stefan.pirker@jku.at

Dr. R. Rössler
voestalpine AG
voestalpine-Straße 1, 4020 Linz, Austria

The ORCID identification number(s) for the author(s) of this article can be found under https://doi.org/10.1002/srin.202000214.

DOI: 10.1002/srin.202000214

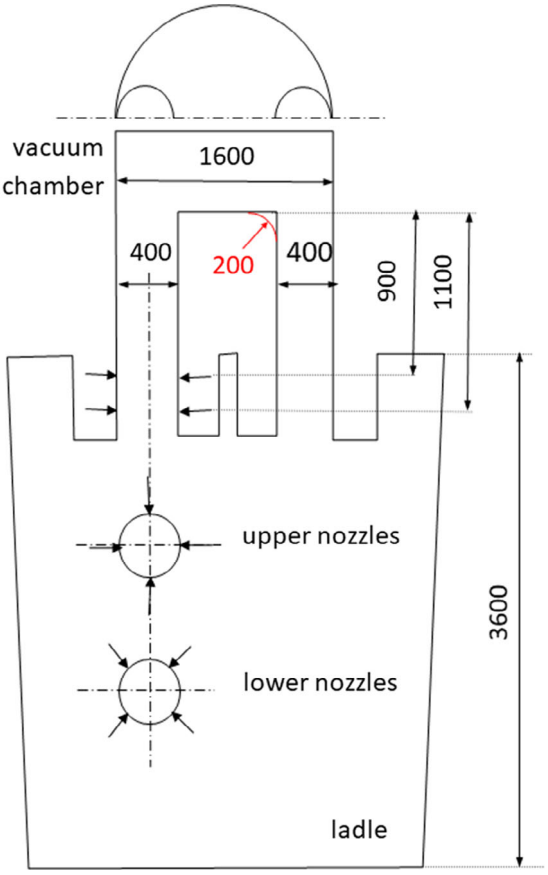

Figure 1. Sketch of a 170 tons RH steel degassing plant; the red line indicates the curve radius used for the rounded edge geometry.

observation of bath surface flow in the VC exhibits a dominantly unsteady flow behavior, which might be prohibitive even for the application of anisotropic URANS turbulence models.

More detailed scale-resolving turbulence models such as the large eddy simulation (LES) method, in turn, require high spatial and temporal resolution which result in excess simulation times, especially in case of long-term processes (such as steel alloy homogenization). In this article, we therefore use recurrence computational fluid dynamics (rCFD) which is a data-assisted methodology for bridging well-separated time scales of fast flow dynamics and comparably slow process dynamics.[12,13]

Generally, rCFD resembles a twofold simulation approach. In the first part, conventional simulation techniques are used to establish a database of characteristic flow patterns, whereas in the second part, rCFD uses this data to efficiently model passive transport processes.

Over the past years, two main classes of rCFD have been developed. In a first flow-based version of rCFD, snap shots of Eulerian flow fields are stored into the database. Subsequently, sequences of those snapshots are stitched together by a recurrence process, yielding an artificial flow which runs beyond the time span covered by the database. On top of this artificial flow, long-term passive transport is represented by conventional transport equations. Typically, this flow-based rCFD methodology

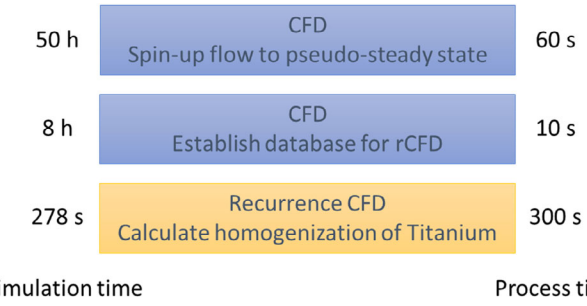

Figure 2. Overall workflow for rCFD simulations. Once conventional CFD simulations show pseudoperiodic flow (i.e., after the initial spin-up process of the flow), characteristic flow pattern are collected into a database in a second step. Finally, rCFD uses these data to simulate titanium transport and homogenization, whereas conventional CFD simulations require large computational times, rCFD actually runs faster than the real-world process itself.

results in a computational speed-up of two orders of magnitude if compared with full CFD simulations.[12,14]

In a second transport-based version of rCFD, snap shots of Lagrangian cell-to-cell communication patterns are stored instead of flow fields. In this case, applying a recurrence process yields a time-varying cell-to-cell communication network, which operates on the computation grid. Based on these communication patterns, passive transport is modeled by convective cell-to-cell shifts of information together with diffusive face swaps of information. In previous studies,[15,16] we showed that this version of rCFD is extremely performant, resulting in a computational speed-up of up to four orders of magnitude, which, in many cases, enables real-time simulation of passive transport on high-resolution grids. The overall workflow of recurrence CFD (rCFD) simulations is shown in **Figure 2**.

Although rCFD is still in development, different versions of rCFD have already been applied successfully to turbulent single-phase flow,[15–18] bubble columns,[12] and fluidized beds.[14,19–21]

In the first part of this article, we present conventional CFD simulations of steel recirculation flow in an RH plant. By opposing our numerical results to real-plant observations of flow fields in the VC, we compare the predictive capabilities of simple RANS models to those of LES turbulence models. We further relate our CFD predictions of global steel recirculation rate (i.e., the mass flux of steel into the VC) to empirical correlations from the literature. In the second part of this article, we proceed with transport-based rCFD simulations of titanium homogenization. Finally, we compare those real-time predictions with plant trials of ferrotitanium addition.

Overall, this article aims to answer two main questions: 1) Can we reliably model the steel recirculation flow in an RH plant? 2) How can we reduce both the expenditures and the costs of such simulations?

2. Modeling: Conventional CFD Simulations

In our previous study, we investigated the dynamic interaction of bubble plumes with a free bath surface by considering sloshing in a spring mounted vessel.[22] In that study, we experienced excellent agreement between experiments and numerical

simulations, combining 1) a VoF model for the bath surface with 2) a DPM for the bubble plumes and 3) a LES model for the turbulence. In this article, we follow the same modeling strategy because the RH process comprises similar flow phenomena of interest. Because modeling details are already given in our previous study,[22] we just outline this modeling concept within the next subsections for the sake of completeness.

2.1. Governing Flow Equations

To resolve the free surface motion in the VC, the VoF model is used, which is based on a transport equation for the phase volume fraction α_q,

$$\frac{\partial \alpha_q \rho_q}{\partial t} + \nabla \cdot (\alpha_q \rho_q \mathbf{u}) = 0 \tag{1}$$

with the phase volume fractions, α_q, summing up to one, $\sum_q \alpha_q = \alpha_l + \alpha_g = 1$. Indices l and g refer to the liquid and the gas phase, whereas the index q represents a general phase with density ρ_q. The mixture velocity $\mathbf{u}$ is subject to a momentum equation

$$\frac{\partial (\rho \mathbf{u})}{\partial t} + \nabla \cdot (\rho \mathbf{u}\mathbf{u}) = -\nabla p + \nabla \cdot \boldsymbol{\tau} + \rho \mathbf{g} + \mathbf{K}_{b \to l} \tag{2}$$

with the phase averaged density $\rho = \sum_q \alpha_q \rho_q$, pressure p, the stress tensor $\boldsymbol{\tau}$, the vector of gravitation $\mathbf{g}$, and the driving force of the bubble plumes $\mathbf{K}_{b \to l}$. The shear rate tensor further follows to

$$\tau = \mu_{t,sg} (\nabla \mathbf{u} + \nabla \mathbf{u}^T) \tag{3}$$

where $\mu_{t,sg}$ denotes either the turbulent viscosity or the subgrid viscosity.

In case of the standard k–ε turbulence model, we insert

$$\mu_t = C_\mu \rho \frac{k^2}{\varepsilon} \tag{4}$$

where k and ε are the specific turbulent kinetic energy and the specific dissipation rate, respectively, and $C_\mu = 0.9$ is model constant.

In case of standard Smagorinsky LES, the subgrid viscosity reads

$$\mu_{sg} = 2(C_s \Delta_{gr})^2 \dot{\gamma} \tag{5}$$

where Δ_{gr} denotes the local grid spacing, $\dot{\gamma}$ the local shear rate (i.e., the second invariant of the shear rate tensor), and $C_s = 0.1$ is a model constant.

2.2. DPM

In the up-leg of the RH plant, our model should be able to represent highly turbulent bubble plumes with significantly varying bubble volume fractions. In accordance with our previous study,[22] we chose a combination of the drag models of Ishii and Zuber and Schiller and Naumann in combination with a swarm adaption. In this model, the overall drag coefficient C_D reads

$$C_D = \beta C_{D,\text{Ishii}} + (1 - \beta) C_{D,\text{Schiller}} \tag{6}$$

where β represents a coupling parameter which depends on the local liquid volume fraction (further details are given by Pirker et al.[22]).

Based on this efficient drag coefficient, the volumetric interaction force between the dispersed bubble phase and the continuous liquid phase reads

$$\mathbf{K}_{b \to l} = C_D \rho \frac{\alpha_l \alpha_b}{L} |\mathbf{u} - \mathbf{u}_b| (\mathbf{u} - \mathbf{u}_b) \tag{7}$$

where indices b and l indicate bubbles and liquid phase, respectively.

Discrete parcels of bubbles are introduced at the submerged nozzles with an initial velocity of $u_n = 100\,\text{m}\,\text{s}^{-1}$, a constant bubble diameter of $d_b = 10\,\text{mm}$. We adjusted the bubble per parcel loading $N_{b/p} = \dot{Q}_{\text{nozzle}} \Delta t_{\text{sim}} / 5 V_b$ such that within each simulation time-step five parcels of bubbles are introduced per nozzle (with $\dot{Q}_{\text{nozzle}}$ being the volumetric flow rate of each nozzle and V_b describing the bubble volume). Once bubbles reach the bath surface, they are deleted.

2.3. Species Transport

On top of this multiphase flow simulation, we consider the transport of dissolved steel alloys by a passive transport equation for the alloy concentration c,

$$\frac{\partial (\rho_l \alpha_l c)}{\partial t} + \nabla \cdot (\rho_l \alpha_l c \, \boldsymbol{u}) = \nabla \cdot \rho_l \alpha_l \Gamma \nabla c + S_c \tag{8}$$

where Γ is the diffusion coefficient and S_c represents local sources due to alloy addition. In this study, we neglect the process of alloy dissolution, assuming that dissolution happens nearly immediately.

2.4. Numerical Settings

We discretized the computational domain including steel ladle, VC, and free board (as shown in Figure 1) by 3.2M purely hexahedral grid cells.

Conventional CFD simulations were performed with the commercial software ANSYS Fluent.[23] Hereby, we adapted the standard DPM by user-defined functions (UDFs) for the swarm drag law. We further applied a user-defined scalar transport equation to picture the transport of dissolved steel alloys.

After spinning up the flow for 60 s, we started with the evaluation of steel recirculation rate, averaging for another 30 s. Due to the highly dynamic flow pattern, very small time steps in the order of $\Delta t = 10^{-2}\,\text{s}$ had to be applied, resulting in an overall simulation time for this 1.5 min process time of approximately 75 h on 24 Advanced Micro Devices (AMD) cores.

3. Results: Conventional CFD Simulations

3.1. Unsteadiness and Secondary Flows

In the vacuum treatment plant of voestalpine Linz, a video camera is installed in the VC, which enables a visual observation of a restricted portion of the bath surface (**Figure 3**b,c). During

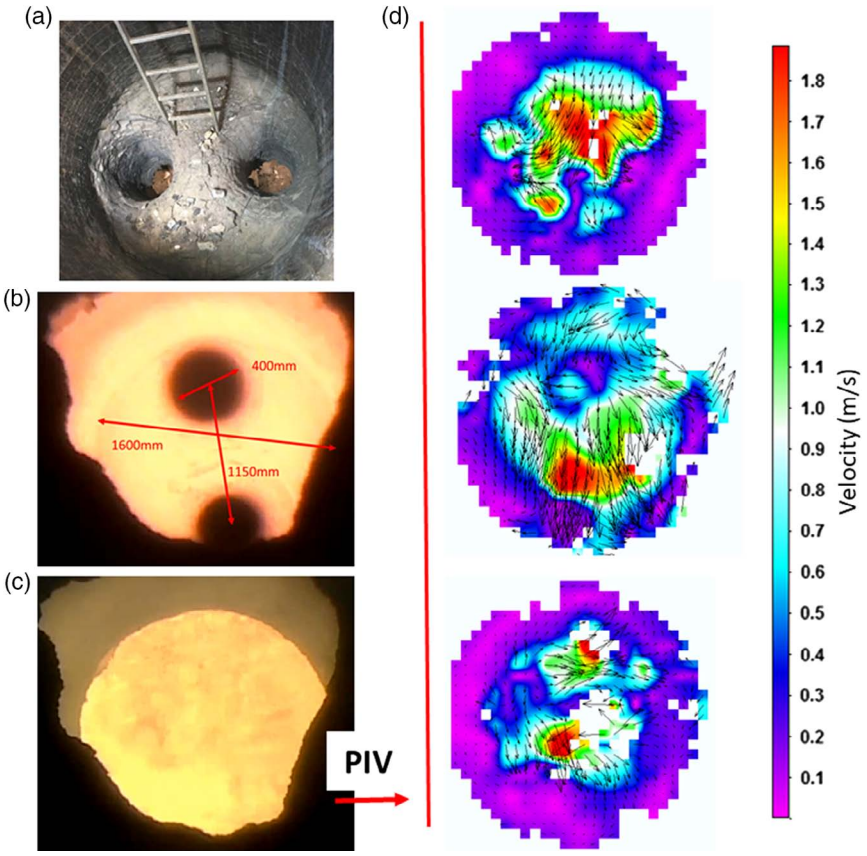

Figure 3. Plant observations at voestalpine Linz: a) photo of VC showing plant erosion patterns after several treatments; b) video snap-shot of VC directly after treatment; c) video snap-shot of VC bath flow showing luminosity patterns; d) PIV evaluations of these luminosity patterns at three instances of time (evaluated during removal of hydrogen operation).

operation, this video coverage reveals highly unsteady brightness patterns at the bath surface, which manifest in visually distinguishable moving dark stripes at the overall bright bath surface. We associate the movement of those stripes to the velocity of the actual steel surface. Based on this assumption, we deduce quantitative velocity fields of the bath surface by particle image velocimetry (PIV). State of the art correlation algorithms for PIV are very robust and can provide a good estimation of velocity vectors even if the common rules of thumb for flow tracers cannot be fulfilled (in our case, the only "tracers" available are the surface stripes and speckles mentioned previously). The presented PIV vector fields are indeed an extreme case of applying PIV cross-correlation techniques and the accuracy of the obtained results cannot be calculated precisely as a calibration beyond the geometry of the VC is not possible. However, Figure 3 shows that it is in fact possible to obtain instantaneous vector fields from video recordings in such harsh environments.

In Figure 3d, three bath surface velocity patterns are exemplified. Obviously, the movement of the bath surface in the VC is dominantly unsteady, exhibiting very irregular flow pattern of significant velocity magnitude of up to $1.8\,\mathrm{m\,s^{-1}}$.

In addition to plant observations, we performed numerical simulations of the steel flow.

Numerical predictions of steel velocity at a horizontal surface close to the bath surface in the VC are shown in **Figure 4**. Obviously, a conventional CFD simulation based on standard URANS turbulence modeling predicts a very regular flow pattern. This flow prediction is characterized by two wall jets, which emit from the up-leg and flow toward the down-leg in a symmetric fashion. In contrast to that, LES turbulence modeling predicts a highly irregular flow pattern as shown in Figure 4b.

By just qualitative comparison with the on-plant measurements, we conclude that an LES-based CFD simulation captures the physical behavior of the steel flow in the VC better than a comparable URANS-based model using the same grid size (of more than 3.2M cells) and time-step width (10 ms).

Actually, this topological difference in the predicted flow patterns in the VC has significant consequences for the flow in the down snorkel and subsequently the global flow in the steel ladle. As shown in **Figure 5**a,b, the LES model predicts significant flow rotation (of alternating spin direction) in the down-leg, whereas the URANS model shows nearly no secondary flow at all. In the steel ladle, the URANS simulation pictures a straight downward jet with all momentum aligned to the jet direction, whereas in case of LES, a rotating jet enters the steel ladle. In comparison with URANS, this jet rotation (of LES) leads to enhanced jet dispersion and consequently less jet penetration.

At this point, we conclude that there are significant differences in the global flow topologies as predicted by URANS simulations and LES, respectively. Furthermore, by comparison with plant

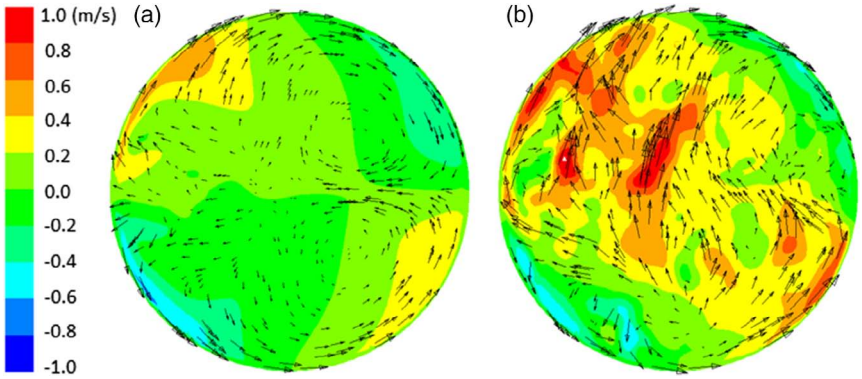

Figure 4. Steel velocity as result of conventional CFD simulations in a horizontal plane close to the bath surface in the VC: a) RANS and b) LES-based turbulence modeling; color indicates *y*-velocity (perpendicular to the plane spanned by the two snorkels) and arrows indicate instantaneous direction of velocity (only every 10th vector is plotted).

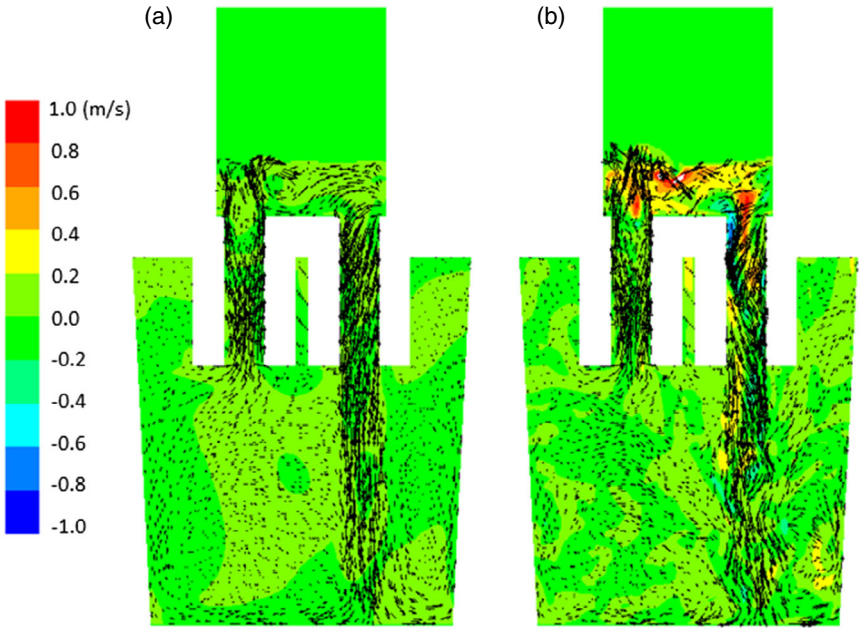

Figure 5. Steel velocity as result of conventional CFD simulations in a vertical plant: a) URANS and b) LES-based turbulence modeling; in contrast to URANS, LES predicts a dominant downward jet with significant secondary rotation; see Figure 4 for color coding.

observation, we suggest that LES are more likely to represent the physics of the steel flow than URANS-based simulations.

3.2. Global Steel Recirculation

In a next step, we therefore proceed with a set of LES simulations of steel recirculation for the evaluation of the average recirculation rate in dependence of the purging gas injection rate. In **Figure 6**, simulation results are depicted by the symbols, with closed symbols indicating mean values (averaged over 30 s) and the triangles indicating minimum and maximum values. In this representation, both—gas purging rate and steel recirculation rate—are normalized by the values of a reference case for which absolute values are shown in **Table 1**. In addition to the simulation results, additional lines highlight the main dependencies given by three empirical correlations. In this case, our LES simulation results agree very well with the predictions of Wei and Yu.[2]

Considering the absolute values shown in Table 1, our numerical simulations predict a smaller mean steel recirculation rate than suggested by the empirical correlation of Wei and Yu.[2] At this point, it might be worth looking at the actual real-plant geometry. Figure 3a shows a typical erosion pattern inside a VC after several treatments. Obviously, the initially sharp edges at the entry of the down-leg have been eroded to a rounded shape (plant operators report that this rounding happens at an early stage of operation, meaning that sharp edges just do not survive even few treatments). In contrast, if we consider a rounded down-leg entry (with a curve radius of 200 mm), LES predicts an increase in mean steel recirculation rate by 15%, which then

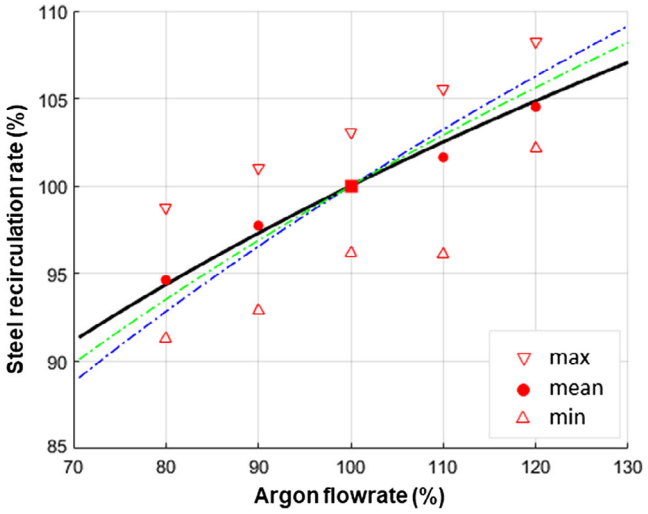

Figure 6. Normalized steel recirculation rate as a function of argon purging rate; symbols indicate results of conventional LES-based CFD simulations (mean, min, and max values), whereas lines show correlations from (solid line) Wei and Yu,[2] (dashed line) Ono et al.,[3] and (dashed–dotted line) Kuwabara et al.[1]

Table 1. Mean steel recirculation rate at a reference gas injection rate of $\dot{Q}_{gas} = 86\,Nm^3\,h^{-1}$ as result of conventional LES-based CFD simulations (with sharp and round down-leg entry) and three empirical correlations; results are given in $kg\,s^{-1}$.

CFD sharp	CFD round	Ono et al.[3]	Kuwabara et al.[1]	Wei and Yu[2]
1030	1184	1092	1205	1150

slightly overestimates the prediction of Wei and Yu. Although both—LES and plant observation—suggest that the erosion pattern in the VC has a significant effect on the steel recirculation rate, none of the considered empirical correlations takes it into account.

At this point, we conclude that CFD simulations based on LES turbulence modeling has the potential to reproduce the flow behavior in alignment with plant observation and available empirical correlations. At the same time, we conclude that these LES are very expensive by means of computational costs requiring days of simulation time for just 1 min of process time (i.e., 50 h computation time for 1 min process time on 24 AMD cores). In the second part of this article, we therefore aim to reduce the computational costs of LES-based CFD simulations by means of data-assisted rCFD.

4. Modeling: rCFD Simulation

The main concept of transport-based rCFD has been published in Pirker and Lichtenegger (in that publication, even algorithmic flow sheets are provided).[15] Further details with regard to the modeling of physical diffusion are given in the literature.[18,19] At this place, we therefore just present the main modeling features and abstain from a detailed description of the rCFD methodology.

4.1. Recurrence Database

In a first step, conventional CFD simulations of pseudoperiodic steel flow (i.e., after recirculation spin-up) feed a database of cell-to-cell communication. For this purpose, buoyant-neutral fluid tracers are seeded throughout the computational domain. During one monitoring time step, these fluid tracers are tracked and their start and end cell IDs are stored into the database. After one monitoring time step, these pairs of cell IDs are stored into one frame of the database together with a weighting scalar, representing the steel volume fraction of the start cell at the beginning of the monitoring step. After one monitoring time step (which in our case is 10 times larger than the time-step of the CFD simulation), another set of fluid tracer is seeded and the process of cell-to-cell communication monitoring starts again. In our case, we filled the database with 100 frames of consecutive cell-to-cell communication patterns covering a total monitoring duration of 10 s.

4.2. Recurrence Process

In a second step, we use a recurrence process, to extrapolate this recurrence database into a continuing thread of time-varying cell-to-cell communication patterns. To start with, we replay an arbitrary sequence of communication pattern, from frame i to frame $j > i$, with random number of frames in between i and j. When the replaying sequence reaches end frame j, we look for a similar frame to serve as start frame for the next replaying sequence. To evaluate the degree of similarity between two frames, we exploit a global recurrence norm, which, in our case, sums up local differences in velocities above a threshold velocity of $|\mathbf{u}|_{min} = 0.5\,m\,s^{-1}$ (by applying this threshold velocity, we focus on only the most dominant flow features). If we plot a recurrence matrix of pairwise global recurrence norms (with frame numbers spanning the two indices, see **Figure 7**), similar frames manifest as local minima in the off-diagonal region of the matrix. After we have chosen a new start frame, we replay a second sequence of communication pattern and so forth.

4.3. Propagation of Information

In a third step, this continuing thread of cell-to-cell communication patterns is used to propagate information of a passive scalar quantity. At its core, one propagation steps consists of two main operations, cell-shifts and face-swaps.

During cell-shifts, passive information, which is stored at individual cells of the computational grid, is shifted to other cells by means of the cell-to-cell communication pattern of the current frame of the recurrence process. Intuitively, one can associate this cell-shift operation to physical convection. To get smooth and complete field information after cell-shifts, averaging (in case several cells are hit) and hole-filling (in case individual cells have not been hit) have to be applied.

Face-swaps, in turn, operate just on neighboring cells such that a portion of information is shifted from the higher-value cell to the lower-value cell. Obviously, this operation is intended to address physical diffusion. Finally, another set of mass-acting face-swaps is used to control the global species balance

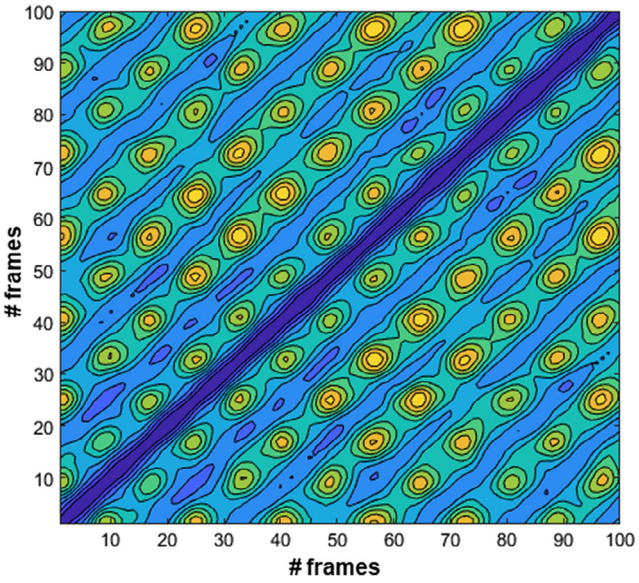

Figure 7. Recurrence matrix showing the normalized recurrence norm for 100 frames in the database; color indicates the degree of pairwise similarity ranging from zero (equal frames) to red (maximal distance between two frames).

(in Pirker and Lichtenegger,[15] this is labeled "global balance safety belt").

Altogether, this way of information propagation on a time-varying communication network represents an extremely simple and performant way of modeling passive transport in the context of CFD.

4.4. Numerical Implementation

All functionalities of rCFD (i.e., the establishment of the recurrence database, the recurrence process, and the propagation steps) have been implemented in ANSYS/Fluent[23] by means of UDFs using message passing interface parallelization. It should be noted that once the database has been established, no solver functionality of ANSYS/Fluent is needed anymore and rCFD acts as a stand-alone software, linked to the UDFs.

5. Results: rCFD Simulations

Figure 7 shows the recurrence matrix for the steel flow inside the RH plant, depicting the pairwise difference of individual frames of the database. Obviously, this matrix has a zero diagonal, meaning that individual frames do not differ at all, if compared with themselves. In the off-diagonal region, however, regular patterns can be seen with lower (bluish) values hinting to frame pairings with significant similarity (which subsequently can be used in the recurrence process).

A closer inspection of this pronounced pseudoperiodic behavior reveals that our conventional CFD predicts regular bubble plume eruptions in the up-leg of the RH plant. In other words, the driving gas pump seems to work in slugging mode.[24] While this pronounced regularity might be attributed to numerical reasons such as the choice of constant bubble diameter, regular eruption of the bubble plumes above the up-leg are also visible by the video coverage of the real plant. By just visual observation, we could estimate the real-plant eruption frequency to be in the order of $f_{\text{plant}} = 1\,\text{Hz}$, whereas our conventional CFD predicts a lower frequency of about $f_{\text{CFD}} = 0.5\,\text{Hz}$.

To study the addition and transport of titanium, we just mark a specific spherical subregion of the bath in the VC with a corresponding initial concentration of already dissolved titanium. After this simplified initialization, information on titanium concentration is propagated on the computational grid by means of rCFD simulations.

In **Figure 8**, the instantaneous concentration of titanium is given in a vertical and three horizontal observation planes for three instances of time $t = 5, 20, 60\,\text{s}$. Due to the highly turbulent motion of the bath, titanium is dispersed in the VC nearly immediately. Already after 5 s, titanium seems to be homogenized in the VC, whereas a first jet of titanium is entering the ladle. The next set of concentration plots at $t = 20\,\text{s}$ exhibits the flow topology inside the ladle, picturing the downward jet together with the upward steel flow at the ladle walls. Finally, the concentration plots at $t = 60\,\text{s}$ indicate that homogenization in the ladle is nearly completed except for some stagnant zones on the top of the ladle, which are hardly affected by the global steel recirculation.

Based on these high-resolution field data, histograms of titanium concentration are deduced in **Figure 9**. Such time-varying

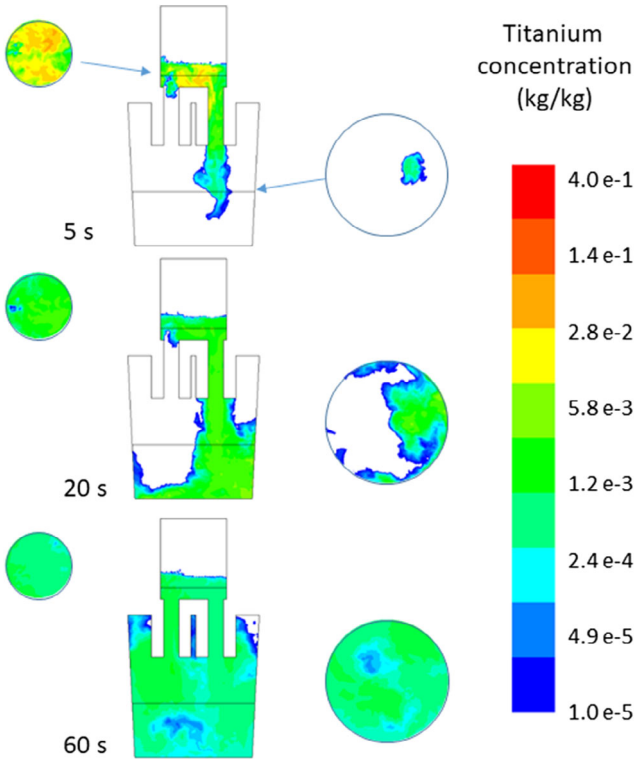

Figure 8. Titanium concentration in the steel as result of rCFD simulations in four observation planes at three instances of time at $t = 5, 20, 60\,\text{s}$ (top to bottom); concentration values are given in logarithmic scale.

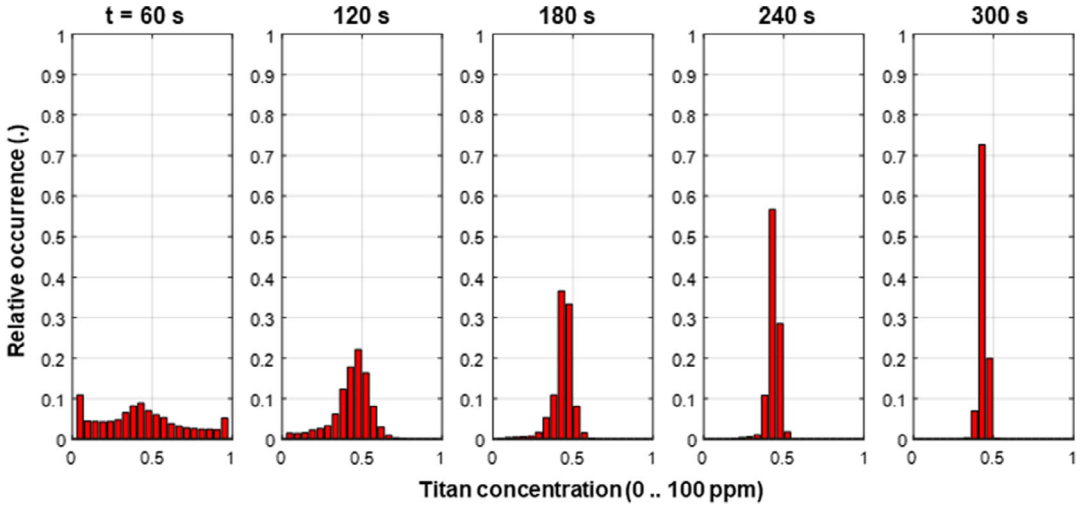

Figure 9. Histograms of titanium concentration in the steel ladle as result of rCFD simulations for five instances of time.

histograms can be used to evaluate the global progress of steel alloy homogenization.

While a direct comparison between conventional CFD and rCFD has already been presented by Pirker and Lichtenegger,[15] we here oppose rCFD predictions to corresponding plant data. In **Figure 10**, dashed lines represent rCFD predictions of the time-varying titanium concentration at the real-plant probe position (in a mid-plane between the snorkels with an immersion depth of approximately 500 mm) and its symmetric counterpart position. While both, the geometry and the titanium initialization, are truly symmetric, the resulting flow exhibits large-scale asymmetric flow features, which leads to different concentrations at these positions (indicated by the two dashed lines). In addition to the concentration at the probe positions, the predicted mean concentration (i.e., the total mass of titanium divided by the total mass of steel) in the ladle is given by the solid line.

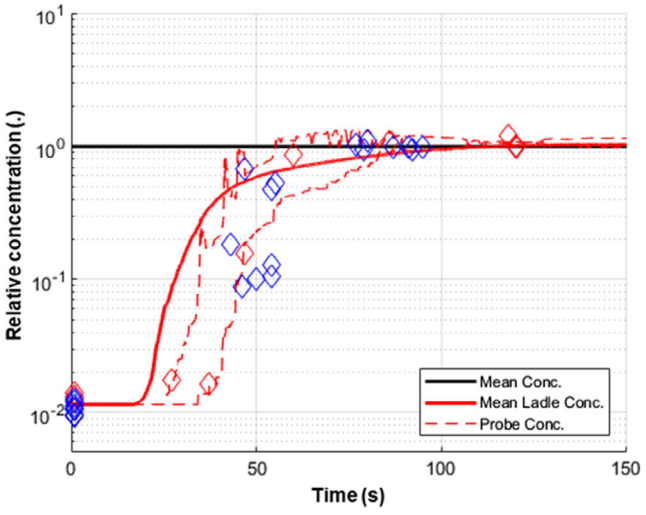

Figure 10. Time evolution of normalized titanium concentration as result of rCFD simulations (lines) and plant trials (symbols); mean values (solid line) and probe values (dashed lines and symbols).

In general, rCFD predictions agree with corresponding real-plant concentration measurements (given by symbols) fairly well. The slight over estimation of titanium homogenization time might be related to our simplified assumption of immediate dissolution of the added ferrotitanium.

Both plant probes and rCFD simulations indicate that steel alloy homogenization is achieved after about 1 min. At an intermediate time of $t = 30$ s, we observe a significant scattering of concentration values (for both measurements and simulations). In this phase of homogenization, the actual concentration values at a given probe position strongly depend on the instantaneous flow pattern and one generally cannot deduce information on the global mean concentration from just these point values. In contrast to just point values, rCFD can provide more reliable (less scattered) field information of titanium concentration to estimate the global mean concentration.

Overall, we experienced that rCFD dramatically improves the computational efficiency. In agreement with previous studies, we experienced a computational speed-up of about four orders of magnitude (i.e., rCFD is 10 000 times faster than conventional CFD). In our case, rCFD was even faster than the corresponding real-world process itself.

We conclude that rCFD can be used for accelerating conventional CFD simulations. Even if rCFD does not add any physics on top of conventional CFD, its fast (real-time) prediction capability might provide new insights for long-term processes. In future, rCFD might also serve as an online prediction tool for high-resolution flow in the context of virtual plant shadows.

6. Conclusion

In this study, we reported on numerical simulations of steel recirculation flow in an RH vacuum treatment plant. Our main findings of conventional CFD simulations are as follows:

The proposed modeling framework (i.e., the combination between a DPM for the bubble plumes and a VoF model for

the free surface in the VC) works numerically stable and produces reasonable results.

While LES turbulence model predicts bath surface motion in the VC in alignment with PIV analysis of on-plant observations, a URANS standard $k-\varepsilon$ model fails to predict those real-plant flow patterns.

LES predicts a different global recirculation topology than corresponding RANS $k-\varepsilon$ simulations. While LES predicts a rotating downward jet emerging into the steel ladle, RANS $k-\varepsilon$ does not show secondary flows. This, in turn, results in different prediction of jet dispersion pattern.

LES predicts the same functional dependency of argon injection rate on steel recirculation rate as proposed by the empirical correlation of Wei and Yu.[2]

A rounded geometry results in higher recirculation rates. Assuming a curve radius of 200 mm at the entry of the down-leg increases the recirculation rate by 15%. In real plants, such roundings inevitably establish after only few treatments.

While LES based on a sharp-edged geometry underestimate steel recirculation if compared with available empirical correlations, an LES based on a rounded geometry leads to good agreement.

In a second part of this article, we applied rCFD to study the transport and homogenization of steel alloy. Our main findings of this part are as follows:

A recurrence analysis of conventional CFD reveals a nearly periodic flow field in the up-leg of the RH plant, suggesting that the gas lift operates in slugging mode. Also, in the real plant, reoccurring eruptions above the up-leg can be observed—however with higher frequency and less regularly.

The transformation of conventional CFD into a data-assisted rCFD works numerically stable and produces reasonable results.

By means of rCFD, we can picture the process of dissolved titanium transport and homogenization, yielding a plausible evolution of high-resolution field information of titanium concentration in the VC and the steel ladle.

The predictions of rCFD simulations are in good agreement with corresponding plant trials of titanium homogenization.

In our case, rCFD was 10 000 times faster than conventional CFD. Although we run rCFD on a grid of 3.2M cells, we could yield time-varying, high-resolution field data of titanium concentration faster than in real-time.

Acknowledgements

The authors acknowledge the support of the COMET Center K1MET as well as the Linz Institute of Technology.

Conflict of Interest

The authors declare no conflict of interest.

Keywords

computational fluid dynamics, recurrence computational fluid dynamics, Rheinsahl–Heraeus plant

Received: April 21, 2020
Revised: May 18, 2020
Published online:

[1] T. Kuwabara, K. Umezawa, K. Mori, H. Watanabe, *Trans. Iron Steel Inst. Jpn.* **1988**, *28*, 305.
[2] J. H. Wei, N. W. Yu, *Steel Res.* **2002**, *73*, 135.
[3] K. Ono, M. Yanagida, T. Katoh, M. Miwa, T. Okamoto, *Denki-Seiko Electr. Furn. Steel* **1981**, *52*, 149.
[4] Y. G. Park, K. Yi, S. Ahn, *ISIJ Int.* **2001**, *41*, 403.
[5] S. Pirker, K. Forstner, *Steel Res. Int.* **2008**, *79*, 591.
[6] L. Lin, Y. Bao, F. Yue, L. Zhang, H. Ou, *Int. J. Miner. Metall. Mater.* **2012**, *19*, 483.
[7] L. Zhang, F. Li, *JOM* **2014**, *66*, 1227.
[8] D. Geng, J. Zheng, K. Wang, P. Wang, R. Liang, H. Liu, H. Lei, J. He, *Metall. Mater. Trans. B* **2015**, *46*, 1484.
[9] H. Ling, F. Li, L. Zhang, A. Conejo, *Metall. Mater. Trans. B* **2016**, *47B*, 1950.
[10] D. Tembergen, J. Schlüter, H. Odenthal, *Stahl und Eisen* **2009**, *129*, 41.
[11] S. Pope, *Turbulent Flows*, Cambridge University Press, Cambridge, UK **2000**.
[12] T. Lichtenegger, S. Pirker, *Chem. Eng. Sci.* **2016**, *153*, 394.
[13] T. Lichtenegger, *Int. J. Multiph. Flow.* **2018**, *106*, 125.
[14] T. Lichtenegger, P. Kieckhefen, S. Heinrich, S. Pirker, *Chem. Eng. J.* **2019**, *364*, 562.
[15] S. Pirker, T. Lichtenegger, *Chem. Eng. Sci.* **2018**, *188*, 65.
[16] S. Pirker, T. Lichtenegger, *Chem. Eng. Sci.* **2019**, *198*, 241.
[17] S. Abbasi, S. Pirker, T. Lichtenegger, *Comput. Fluids* **2020**, *196*, 104348.
[18] Y. Du, B. Blocken, S. Pirker, *Build. Environ.* **2020**, *170*, 106604.
[19] F. Dabbagh, S. Pirker, S. Schneiderbauer, *AIChE J.* **2020**, *66*, 1.
[20] P. Kieckhefen, T. Lichtenegger, S. Pietsch, S. Pirker, S. Heinrich, *Particuology* **2019**, *42*, 92.
[21] T. Lichtenegger, E. Peters, J. Kuipers, S. Pirker, *Chem. Eng. Sci.* **2017**, *172*, 310.
[22] S. Pirker, A. Aigner, G. Wimmer, *Chem. Eng. Sci.* **2012**, *68*, 143.
[23] Ansys Inc., ANSYS Fluent. **2016**.
[24] S. Kassab, H. Kandil, H. Warda, W. Ahmned, *Int. J. Heat Fluid Flow* **2009**, *30*, 88.